Multi-Length Scale Modeling of High-Pressure-Induced Phase Transformations in Soda-Lime Glass

M. Grujicic, W.C. Bell, P.S. Glomski, B. Pandurangan, B.A. Cheeseman, C. Fountzoulas, and P. Patel

Molecular-level modeling and simulations are employed to study room-temperature micro-structural and mechanical response of soda-lime glass when subjected to high (i.e., several giga-Pascal) uniaxial-strain stresses/pressure. The results obtained revealed the occurrence of an irreversible phase-transformation at ca. 4 GPa which was associated with a (permanent) 3-7% volume reduction. Close examination of molecular-level topology revealed that the pressure-induced phase transformation in question is associated with an increase in the average coordination number of the silicon atoms, and the creation of two- to fourfold (smaller, high packing-density) Si-O rings. The associated loading and unloading axial-stress versus specific-volume isotherms were next converted into the corresponding loading Hugoniot and unloading isentrope axial-stress versus specific-volume relations. These were subsequently used to analyze the role of the pressure-induced phase-transformation/irreversible-densification in mitigating the effects of blast and ballistic impact loading onto a prototypical glass plate used in monolithic and laminated transparent armor applications. The results of this part of the study revealed that pressure-induced phase-transformation can provide several beneficial effects such as lowering of the loading/unloading stress-rates and stresses, shock/release-wave dispersion, and energy absorption associated with the study of phase-transformation.

1. Introduction

Several different materials and design strategies are currently being used in transparent blast/ballistic-impact resistant vehicle structures (e.g., windshields, door windows, viewports, etc.). Among the most recently introduced transparent materials and technologies, the following have received the most attention: transparent crystalline ceramics [e.g., aluminum-oxinitride spinel, AlON, sapphire (Ref 1)], new transparent polymer materials [e.g., transparent nylon (Ref 2)], and new interlayer technologies [e.g., polyurethane bonding layers (Ref 3)], and new laminate structure designs (Ref 4). Despite the clear benefits offered by these materials and technologies (e.g., transparent ceramics offer a very attractive combination of high stiffness and high hardness levels, highly ductile transparent polymers provide superior fragment containing capabilities, etc.), ballistic glass remains an important constituent material in a majority of transparent impact resistant structures used today. Among the main reasons for the wide-scale use of glass, the following three are most frequently cited: (a) glass-structure fabrication technologies enable the production of curved, large surface-area, transparent structures with thickness approaching several inches; (b) relatively low material and manufacturing costs; and (c) compositional modifications, chemical strengthening, and controlled crystallization have demonstrated the capability to significantly improve the shock/ballistic impact survivability of glass (Ref 2).

Extensive prototyping and laboratory/field experimental testing is typically required for the development of new glass-based transparent impact-resistant structures aimed at reducing the vulnerability of protected vehicle occupants and on-board instrumentation to various blast/ballistic threats. These experimental efforts are critical for ensuring the utility and effectiveness of the transparent impact-resistant structures. However, these efforts are generally expensive, time-consuming, and involve destructive test procedures. While the role of prototyping/testing programs remains critical, they are increasingly being complemented by the corresponding computation-based modeling and simulation efforts. However, the effectiveness and reliability of the computation-based modeling and simulation approaches is greatly affected by the ability of the associated material models to realistically describe deformation/fracture response of ballistic glass under high-rate/high-pressure loading conditions encountered during blast/ballistic impact. Therefore, one of the main objectives of this study is to further advance the application of computational modeling/simulation-based engineering approaches of transparent impact-resistant structures via the identification and quantification of processes and phenomena occurring in glass under high-pressure/high-strain rate loading conditions as encountered during blast/ballistic impact.

A comprehensive literature review carried out as part of this study revealed that the mechanical behavior of glass is modeled predominantly using three distinct approaches: (a) molecular-modeling methods; (b) continuum-material approximations,

M. Grujicic, W.C. Bell, P.S. Glomski, B. Pandurangan, B.A. Cheeseman, C. Fountzoulas, and **P. Patel,** Department of Mechanical Engineering, Clemson University, Clemson, SC 29634-0921. Contact e-mail: gmica@clemson.edu.

and (c) models based on explicit crack representation. A brief overview and the main findings for each of these three approaches are given below.

Within the molecular modeling methods, glass is treated as an assembly of discrete particles (atoms and ions) which interact with each other via the so-called inter-atomic (or force field) potentials. By employing different mechanics and dynamics schemes, these models can provide a fairly accurate assessment of various glass properties such as elastic constants, strength, chemical and thermal diffusivities, surface energies, etc. Of interest to this study, a great number of researchers have investigated, using molecular modeling techniques, the propensity of various types of glass (of different chemistries and microstructures) to undergo phase transformations when subjected to high hydrostatic pressures on the order of several GPas (Ref 5-8). The emphasis in these investigations was placed on elucidating the predominant atomic-level mechanisms and processes (e.g., increased coordination number, often referred to as *coordination defects*, creation of new metastable chemical bonds, etc.) associated with the phase transformations in glass. In this study, on the other hand, molecular-modeling investigations of high-pressure micro-structure and behavior of soda-lime glass are carried out to predict the continuum-level mechanical response of this material when subjected to blast/ballistic impact loading conditions. Specifically, the potential of the observed high-pressure phase-transformation/irreversible densification for blast/ballistic impact mitigation is analyzed.

Within the continuum-level glass models (Ref 9-15), glass is treated as a continuum material whose stiffness and strength properties may become degraded by nucleation, growth, and coalescence of cracks. The fundamental assumption in these models is that the elastic-stiffness and strength degradations are the result of inelastic deformation caused by micron and sub-micron size cracks, and that this degradation can be quantified using a so-called damage tensor whose evolution during loading can be formulated using generalized Griffith-type crack initiation and propagation criteria for brittle materials. In addition, some continuum models account for the interactions between the cracks, their coalescence, friction between fragments, competition between micro-cracking leading to fine-scale fragmentation of glass and macro-cracking giving rise to coarse fragmentation, etc. (Ref 16).

Within the explicit crack representation material model framework, glass is treated as a linear elastic material, and its fracture is considered to take place via nucleation, propagation, and coalescence of discrete (rather than smeared-out/homogenized) cracks during impact (Ref 17). In other words, while within the continuum modeling framework the stiffness/strength-degrading effect of smeared-out cracks is included only implicitly, in the explicit crack representation cracks are considered as discrete entities and their effect on material stiffness/strength is accounted for explicitly. When the latter type of glass models are implemented into a finite element computational framework, crack nucleation and propagation are handled by duplicating nodes at the crack tip/front. Adaptive re-meshing is used to provide a rich enough set of possible fracture paths around the crack tip. As a crack grows, forces at newly cracked (free) surfaces are brought to zero in accordance with the Griffith criterion to account for crack growth-induced unloading. This procedure enables explicit modeling of the crack coalescence processes which can lead to the formation of fragments. The major disadvantage of the discrete models is their propensity to become extremely computationally expensive and become intractable as the number of cracks increases. That is, to capture all possible crack nucleating sites, meshes with micron-size elements are ultimately required. This is the main reason that this type of model is used mainly to study various deformation and fracture processes in glass but are rarely utilized in the computer aided engineering efforts aimed at developing transparent structures with superior blast/ballistic-impact survivability.

As demonstrated above, molecular-level, continuum-level, and discrete modeling are maturing areas of glass research which are capable of revealing complex intrinsic mechanisms and phenomena associated with deformation and fracture in glass. However, these modeling approaches are typically concerned only with the effect of the observed processes/mechanisms on the behavior of glass at their respective length scales, and practically no reports were found where the knowledge about glass behavior at one length scale was used to improve glass models at other length scale(s). Therefore, the main objectives of this study are: (a) to investigate and quantify (using molecular-level modeling and simulation techniques) the high pressure-induced phase transformations in soda-lime glass and the accompanied (irreversible) densification; (b) to use the pressure versus specific-volume loading/unloading isotherms obtained in (a) to construct the corresponding pressure versus specific-volume loading Hugoniots and un-loading isentropes; and (c) to use the Hugoniots and isentropes obtained in (b) to analyze shock propagation within soda-lime glass and the potential of pressure-induced phase-transformation/irreversible densification in mitigating the effects of blast/ballistic impact.

The organization of the article is as follows: a brief description of the molecular-level microstructure of glass including its random-network representation is presented in section 2. Details regarding computational model, the inter-atomic force field potentials, the computational method and the key results relating to the molecular-level modeling and simulation portion of this study are presented in section 3. The procedures used for the conversion of the molecular-level-derived loading/unloading isotherms into the corresponding loading Hugoniots and unloading isentropes and the associated results are presented in section 4. Examination of the potential of the pressure-induced phase transformation/irreversible-densification in mitigating the effects of blast/ballistic impact is discussed in section 5. The key conclusions resulting from this study are summarized in section 6.

2. Molecular-Level Microstructure of Glass

Due to the lack of long range order, glass is referred to as an amorphous material. The molecular microstructure in glass reveals a random distribution of the basic constituents which is quite different than the regular microstructure found in the crystalline materials. The former molecular-level microstructure is typically described using the so-called random network model (Ref 18) which defines glass as a three-dimensional network of oxygen polyhedra (a cation surrounded by three or four oxygen ions) mutually connected through sharing of the vertex oxygen atoms. In the case of silicate-based glasses like soda-lime glass, the polyhedra are mainly SiO_4^{4-} tetrahedra. Elements like silicon, which reside in the center of the polyhedra, are typically referred to as "network-formers" and their valence/coordination-number (four, in the case of silicon)

defines the geometry of the polyhedra (tetrahedron, in the case of silicon).

When alkali (or alkaline earth) oxides are added to a pure silicate glass, the added oxygen ions become incorporated into the silicate network while the metallic cations remain close-by to provide local charge neutrality. For the added oxygen ions to attach to the silicate network, some of the Si-O bonds within the network must be broken. Accommodation of these additional oxygen ions within the network as well as the metallic cations necessitates that the network must become more open. Since alkali (or alkaline earth)-based oxides modify the basic silicate network in glass, they are typically referred to as "network modifiers." Soda-lime glass, which is the subject of the present investigation, contains about 14 wt.% Na_2O and 9 wt.% CaO with both of these oxides acting as network modifiers. In contrast to network modifiers, more-covalent oxides like B_2O_3 donate metallic cations which are directly incorporated into the glass network and that is the reason that these oxides are generally considered as network formers. It should be noted however that due to a lower valence (three, in the case of boron) the nature of the network polyhedra changes locally from silicate tetrahedra to boron-centered triangles. This type of glass network is found in borosilicate glass which is the subject of our on-going investigation.

Within the random network model, it is often convenient to describe the structure of the network in terms of the average number of oxygen ions per network forming ion, typically denoted as R. For single component glasses, such as fused silica (pure SiO_2), R takes on the value of 2.0. In the case of soda-lime glass, the presence of additional oxygen ions in the glass network increases the R value to ca. 2.41. As a general rule of thumb, higher values of R reflect the presence a larger number of oxygen ions per glass-forming ion and lead to a more open, weaker structure. On the other hand, smaller values of R indicate the presence of network formers with a lower coordination number. Depending on the network former coordination number, its concentration, and the strength of its bond with oxygen, varying effects on the morphology of glass network may be observed. In addition to the R parameter, a glass network is often also described in terms of the X and Y parameters which, respectively, define the average number of non-bridging (connected to one glass forming ion) and bridging (connected to two glass-forming ions) oxygen ions per network polyhedron. In fused silica, $X = 4.0$ and $Y = 4.0$ since this glass contains only bridging oxygen atoms. On the other hand, since soda-lime glass contains additional non-bridging oxygen ions, X takes on a non-zero value (ca. 0.81) while Y drops below 4.0 (ca. 3.19).

In addition to the aforementioned changes in the morphology of glass network which are brought about by changes in glass chemistry, similar changes can be induced mechanically (typically requiring several GPa pressure levels). Specifically, at high pressures, the coordination number of the network formers can change resulting in a phase transformation characterized by changes in the geometry of the network polyhedra. The phase transformations in question could be, either, of the first order resulting in the formation of distinct high-pressure phases at a nominally constant pressure or of the second order characterized by gradual evolution of the low-pressure phase to the high-pressure phase over a range of pressures. These phase transformations can be associated with significant volume changes and, since phase-transformation-induced energy absorption is a well-documented phenomenon responsible for

high toughness levels in TRIP steels and partially stabilized crystalline ceramics, it is of interest to this study. It should be noted, however, that the phase-transformations analyzed in this study occur in a pressure-range (ca. 3-5 GPa) consistent with those encountered in typical blast/ballistic impact scenarios or situations and are associated with relatively modest (3-7% volume changes). These phase-transformations should not be confused with the ones taking place at substantially higher pressures (ca. >20 GPa), which are associated with substantially larger volume reductions and with the formation of *stishovite*, an octahedrally coordinated glass phase.

3. Molecular-Level Analysis of Soda-Lime Glass

3.1 Computational Analysis

Formulation of a molecular-level simulation problem requires, at a minimum, specification of the following three aspects: (a) a molecular-level computational model consisting of atoms, ions, functional groups, and/or molecules; (b) a set of interaction potentials (commonly referred to as force fields) which describe accurately various bonding and non-bonding interaction forces between the constituents of the molecular model; and (c) a computational method(s) to be used in the simulation. Further details of these three aspects of the molecular modeling analysis of soda-lime glass are provided below.

3.1.1 Computational Model. At the molecular level, soda-lime glass is modeled as a discrete material consisting of: (a) silicon (Si) and oxygen (O) atoms mutually bonded via a single covalent bond and forming a connected, non-structured/amorphous network of silica (SiO_4^{4-}) tetrahedra; (b) oxygen anions (O^{2-}) attached as terminal functional-groups to the fragmented silica tetrahedra network; and (c) sodium cations (Na^+) dispersed between fragmented silica tetrahedra networks and ionically bonded to the oxygen anions.

While glass is an amorphous material and does not possess any long-range regularity in its atomic/molecular structure, modeling of bulk behavior of glass is typically done at the molecular level by assuming the existence of a larger (amorphous) unit cell. Repetition of this cell in the three orthogonal directions (the process also known as application of the "periodic boundary conditions") results in the formation of an infinitely large bulk-type material. This procedure was adopted in this study.

The cube-shaped computational cell used in this study contained 2,916 particles with an overall chemical composition of $(Na_2O)_{0.15}$ $(SiO_2)_{0.85}$. The unit cell edge-length was set to 3.347 nm yielding a soda-lime glass nominal density of 2.613 g/cm^3. The three edges (a, b, and c) of the cell were aligned, respectively, with the three coordinate axes (x, y, and z).

To create the initial particle configuration in the unit cell, the Visualizer (Ref [19]) program from Accelrys was first used to construct a short silica-chain fragment. The fragment was then "grown" by a duplicate-and-attach process using the same program. The resulting silica network (along with additional sodium cations and oxygen anions) was next used within the Amorphous Cell program (Ref [20]) from Accelrys to randomly populate the computational cell while ensuring that the target material density of 2.613 g/cm^3 was attained. An example of a

typical molecular-level topology within a single unit cell is displayed in Fig. 1.

3.1.2 Force-Fields. To fully account for the bonding and nonbonding types of interactions between the atoms/ions/molecules described in the previous section, one must define the respective interaction-potential functions/force-fields, as well as the associated atomic-polar and ionic charges. The knowledge of such force fields enables determination of the potential energy of a molecular-level system in a given configuration. In general, the potential energy of a system of interacting particles can be expressed as a sum of the valence (or bond), $E_{valence}$, cross-term, $E_{cross-term}$, and non-bond, $E_{non-bond}$, interaction energies as:

$$E_{total} = E_{valence} + E_{cross-term} + E_{non-bond} \qquad (Eq\ 1)$$

The valence energy generally includes a bond stretching term, E_{bond}, a two-bond angle term, E_{angle}, a dihedral bond-torsion term, $E_{torsion}$, an inversion (or an out-of-plane interaction) term, E_{oop}, and a Urey-Bradlay term (which involves

interactions between two particles bonded to a common particle), E_{UB}, as:

$$E_{valence} = E_{bond} + E_{angle} + E_{torsion} + E_{oop} + E_{UB} \qquad (Eq\ 2)$$

A schematic explanation of the first four types of valence atomic interactions is given in Fig. 2.

The cross-term interacting energy, $E_{cross-term}$, accounts for the effects such as bond length and angle changes caused by the surrounding atoms and generally includes: stretch-stretch interactions between two adjacent bonds, $E_{bond-bond}$, stretch-bend interactions between a two-bond angle and one of its bonds, $E_{bond-angle}$, bend-bend interactions between two valence angles associated with a common vertex particle, $E_{angle-angle}$, stretch-torsion interactions between a dihedral angle and one of its end bonds, $E_{end\_bond-torsion}$, stretch-torsion interactions between a dihedral angle and its middle bond, $E_{middle\_bond-torsion}$, bend-torsion interactions between a dihedral angle and one of its valence angles, $E_{angle-torsion}$, and bend-bend-torsion interactions between a dihedral angle and its two valence angles, $E_{angle-angle-torsion}$, terms as:

$$\begin{aligned}E_{cross-term} = {} & E_{bond-bond} + E_{angle-angle} + E_{bond-angle} \\ & + E_{end\_bond-torsion} + E_{middle\_bond-torsion} \qquad (Eq\ 3) \\ & + E_{angle-torsion} + E_{angle-angle-torsion}\end{aligned}$$

The non-bond interaction term, $E_{non-bond}$, accounts for the interactions between non-bonded particles and includes the van der Waals energy E_{vdW} and the Coulomb electrostatic energy, $E_{Coulomb}$, as:

$$E_{non-bond} = E_{vdW} + E_{Coulomb} \qquad (Eq\ 4)$$

In the present molecular-level analysis of soda-lime glass Condensed-phased Optimized Molecular Potential for Atomistic Simulation Studies (COMPASS) (Ref 21, 22) functional forms and parameterizations were used for various bond and non-bond interaction energies appearing in Eq 1-4. COMPASS is a set of force field potentials which were derived through the use of ab initio quantum mechanical calculations and has proven to be highly accurate and reliable in
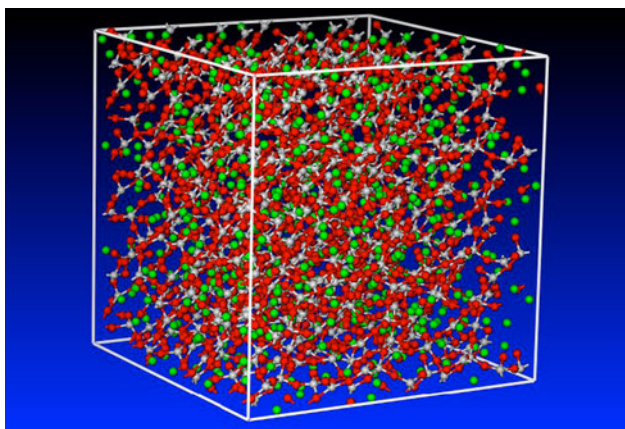

Fig. 1 The computational unit cell for soda-lime glass molecular-level simulations used in this study

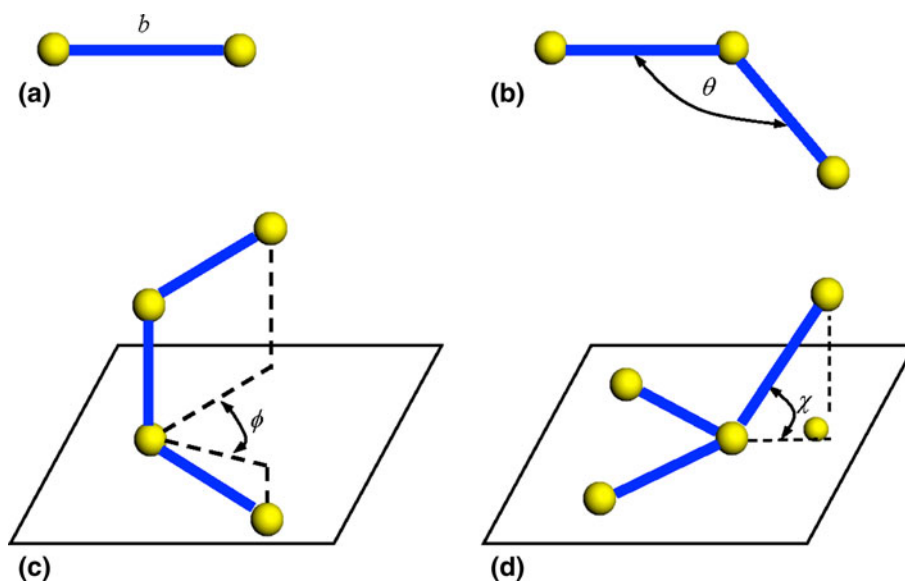**Fig. 2** A schematic of the: (a) stretch, (b) angle, (c) torsion, and (d) inversion valence atomic interactions

starting various organic/inorganic condensed matter problems. A summary of the COMPASS force-field functions can be found in our previous study (Ref 23).

3.1.3 Computational Method. Molecular-level simulations typically rely on one of the following two techniques: (a) molecular statics, the technique within which the potential energy of the molecular structure in question is minimized with respect to the position of the constituent atoms and ions in the unit cell as well as with respect to the size and shape of the unit cell; and (b) molecular dynamics, a technique within which the Newton's equations of motion are solved, as a function of time, for all interacting atoms and ions in the system and the appropriate ensemble averages are used to assess/quantify various molecular-level material properties. Both molecular statics and molecular dynamics methods were employed in this study.

High-pressure-induced phase transformations and the associated densification in soda-lime glass were studied in this study using a conventional *NPT* dynamics method within the Discover program (Ref 24) from Accelrys, where *N* (the number of particles), *P* (pressure), and *T* (temperature) are the system states that are held constant or ramped in a controlled manner during compression-simulation runs. The equations of motion were integrated using the velocity Verlet algorithm with a time step of 1.0 fs. To comply with typical blast/ballistic-impact loading conditions, pressure was ramped linearly at a rate of 0.3 GPa/ps. Pressure ramping was accomplished by 0.1 GPa discrete increments in pressure followed by 10.0 ps equilibration times at a given pressure level. Temperature, on the other hand, was held constant at a value of 298 K using a Nosé Thermostat (Ref 25). Molecular-level microstructure of the soda-lime glass was monitored at different pressure levels as a function of time to detect the onset and quantify the progress of phase transformations.

At the end of equilibration at each pressure level, the average material density (inverse of specific-volume) was computed from the corresponding pair-correlation functions. This procedure yielded the pressure versus specific-volume isothermal relations (*isotherms* in the following) for the pressurization portion of a loading/unloading cycle. To determine the corresponding pressure versus specific-volume relation during the depressurization portion of a loading/unloading cycle, pressure was decreased in a similar manner as discussed above. Differences in the pressure versus specific-volume relations for the pressurization and depressurization portions of the loading cycle are then used to quantify the extent of high-pressure irreversible densification of soda-lime glass.

As will be shown later, high-pressure-induced phase transformations in soda-lime glass can affect the strength of this material. Too assess the extent of such strengthening, molecular-level simple-shear tests were carried out. These tests were conducted through the use of a Discover input file which was written in a Basic Tool Command Language (BTCL). This enabled the use of a scripting engine that provides very precise control of simulation runs, e.g., a cell deformation to be carried out in small steps each followed by a molecular dynamics equilibration step and, in turn, by an energy minimization step. The minimization portion of the molecular-level simple shear tests was carried out using a combination of three (Steepest Descent, Conjugate Gradient, and Newton's) potential-energy minimization algorithms within Discover (Ref 24). These algorithms are automatically activated/deactivated as the molecular-level configuration approaches its energy minimum (i.e., the Steepest Descent method is activated at the beginning of the energy-minimization procedure, while the Newton's method is utilized in the last stages of the simulation).

To determine the strength of soda-lime glass in its virgin (untransformed) and (pressure-induced) fully transformed conditions, the corresponding computational cells are subjected to a sequence of simple-shear deformation modes. The procedure used in our previous study (Ref 26) which relates the (minimum) energy to the first and second invariants of the left Cauchy deformation tensor, evolution of the stress state (including the equivalent stress) during deformation is determined. The observed equivalent-stress plateau is then identified as the material strength.

3.2 Results and Discussion

In this section, a brief summary of the molecular-level computational results pertaining to the response of soda-lime glass subjected to high pressures is provided. While this portion of the study yielded numerous results, only the ones directly related to the potential effect of phase transformations on the continuum-level material model in the high-rate, high-pressure loading regime are presented and discussed in greater detail. A more comprehensive account of the results obtained will be provided in a future communication.

3.2.1 Molecular-Level Topology. A detailed examination of the molecular-level topology after subjecting the unit-cell to high pressures revealed distinct differences depending on whether the maximum pressure was below or above ca. 4 GPa.

Pressures Below ~4 GPa. Molecular modeling of glass pressurization/depressurization revealed that when glass is exposed to pressures not exceeding ca. 4 GPa, no detectable irreversible changes generally take place in its molecular topology. Closer examination of the atomic structure at different pressure levels between 0 and 4 GPa revealed:

(a) The presence of "active regions" within which atoms may occasionally undergo large displacements/jumps (ca. 0.1 nm). These atomic displacements (the results not shown for brevity) were found to involve coordinated motion of at least a dozen atoms and to be accompanied by abrupt changes in the average potential energy;

(b) In most cases, atomic rearrangement described in (a) appears to be associated with low-frequency transition of the active regions between two distinct "equilibrium" states (of comparable potential energy). These findings are in complete agreement with those found by Trachenko and Dove (Ref 7) who termed this phenomenon as Double Well Potential (DWP) and the associated low-frequency transition/vibrational mode as the "floppy mode"; and

(c) While pressurization up to 4 GPa did not yield any permanent changes in the molecular topology, the locations of the active regions were found to change with pressure. That is, the regions active at one pressure level may become inactive at another pressure level while, at the same time other previously inactive regions would become active.

Pressures Above ~4 GPa. When the computational cell is subjected to pressures exceeding ca. 4 GPa and subsequently depressurized to zero pressure, permanent changes in the glass
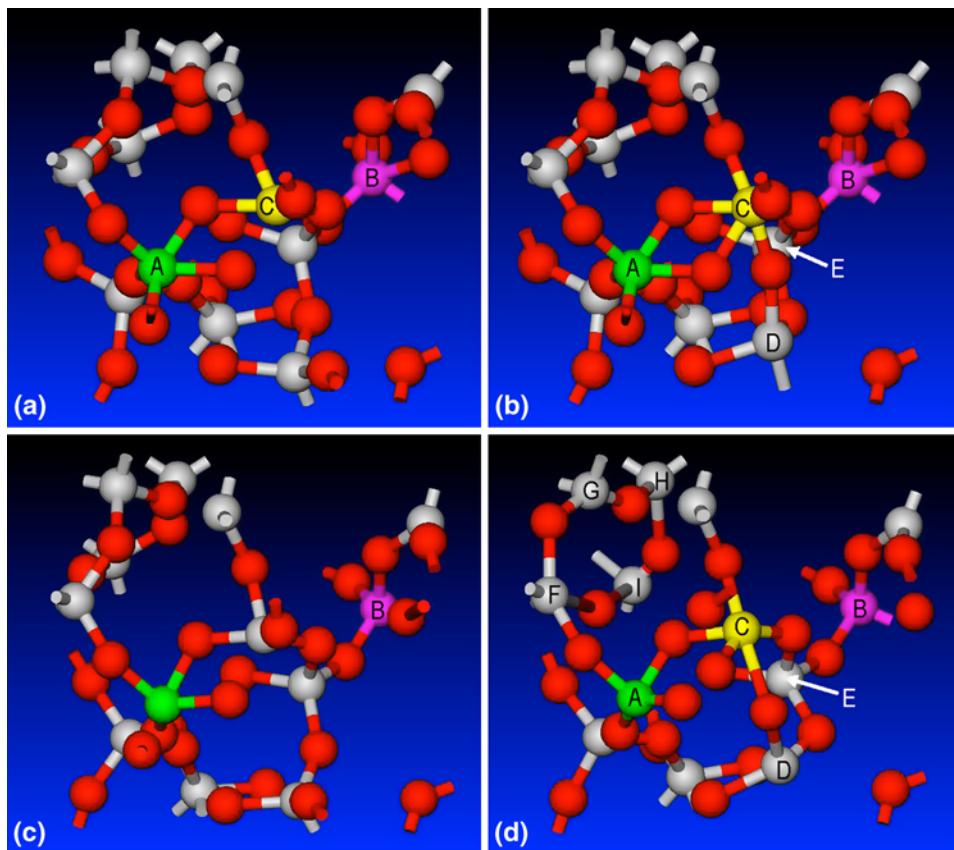
Fig. 3 The molecular level topologies pertaining to: (a) high-pressure state, (b) high pressure state after a prolonged (20 ps) relaxation period, (c) ambient pressure state resulting from depressurization of state (a), and (d) ambient pressure state resulting from depressurization of state (b) (see text for explanation)

molecular topology were normally observed. These molecular topology changes were accompanied by a permanent density increase on the order of 3-7%. An example of typical results obtained in this portion of the study is given in Fig. 3(a-d), where oxygen atoms/anions and silicon atoms are shown, while sodium cations are omitted for clarity. To aid in visualization/interpretation of the topological changes experienced by glass during high pressure loading/unloading cycles, only a 30-40 atom examplary region of computational cell was monitored in Fig. 3(a-d). The molecular level topologies displayed in these figures pertain, respectively to: Fig. 3(a) high-pressure state; (b) high pressure state after a prolonged (20 ps) relaxation period; (c) ambient pressure state resulting from depressurization of state (a); and (d) ambient pressure state resulting from depressurization of state (b). It should be noted that the results displayed in Fig. 3(c) are essentially identical to those in the initial configuration prior to loading. A closer examination of the molecular-level topology results displayed in these figures revealed that:

(a) Pressurization alters not only molecular-level topology, but also changes the bonding structure and increases the average coordination number (of mainly Si atoms). This can be seen by comparing the results displayed in Fig. 3(a) and (c). It should be noted here that the results displayed in Fig. 3(c) are used in place of the initial molecular-level topology results. In these figures, it is seen that silicon atoms labeled *A* and *B* change their

fourfold coordination to fivefold coordination upon pressurization.

(b) As implied earlier, if the depressurization is carried out without allowing the material to relax at high pressures, the molecular level configuration obtained at the ambient pressure is effectively identical to the initial configuration, Fig. 3(c). Thus, in the resultant ambient-pressure configuration, most silicon atoms regain their fourfold coordination.

(c) Increased duration of the exposure of glass to high pressure, results in continued changes in the molecular-level topology and bond structure. This can be seen by comparing the results displayed in Fig. 3(a) and (b). These figures show that relaxation of glass leads to the *C*-labeled silicon atom acquiring a fivefold coordination while, at the same time smaller size Si-O rings are being formed. For example, a twofold ring is formed involving the *A* and *C* silicon atoms, while a threefold ring involving the *C*, *D*, and *E*-labeled Si atoms also appears, Fig. 3(b). These changes in the molecular-level topology of glass are a manifestation of its relaxation to a material state that is energetically preferred at high pressures.

(d) Upon depressurization of glass which was relaxed at high pressures, some changes in the molecular-level topology and the bonding structure are observed. However, the initial material state is not restored. That is, the material has undergone permanent changes in its molecular level topology, bond structure, and density.

This can be seen by comparing results displayed in Fig. 3(c) and (d). These figures show that while *A*- and *B*-labeled silicon atoms regain their fourfold coordination upon depressurization to ambient pressure, the *C*-labeled silicon atom retains its fivefold coordination, Fig. 3(b) and (d). Thus, the average coordination number of silicon atoms in the relaxed-then-depressurized state, Fig. 3(d), is higher than that in the initial configuration, Fig. 3(c). Furthermore, while the aforementioned twofold Si-O ring was broken upon depressurization, the threefold ring involving the *C*, *D*, and *E*-labeled silicon atoms survived this process. In addition, a new fourfold ring involving the Si atoms labeled *F*, *G*, *H*, and *I* was formed. The threefold and fourfold rings were not present in the initial molecular-level configuration, Fig. 3(c).

3.2.2 Pressure Versus Specific-Volume Isotherm. An example of the typical pressure, *p* versus specific-volume, *v* (298 K isothermal) results obtained in the present molecular-level analysis of high-pressure irreversible densification of glass is displayed in Fig. 4. The results in Fig. 4 show four loading pressurization/depressurization cycles. The first cycle does not result in any irreversible densification of glass since the maximum pressure attained is not high enough. The second and third cycles yield irreversible densification and reveal that this process is associated with a nearly constant ca. 4 GPa pressure level. During the last cycle, irreversible densification is completed so that glass behaves as a perfectly elastic material when subjected to any further loading.

To summarize the aforementioned observations, the examination of the results displayed in Fig. 4 revealed the following three important findings: (a) irreversible densification begins at a pressure level of ∼4 GPa and proceeds to full densification at a nominally constant pressure; (b) irreversible densification is associated with a density increase of ca. 3-7%; and (c) the average rate of change of pressure with density (which scales with the material bulk modulus) is not significantly different (and will be assumed equal) in the pre- and post-densification glass states.

It should be noted that the aforementioned findings (a) and (c) were found not to be very sensitive to the random selection of the initial molecular-level configuration of glass. On the other hand, the extent of irreversible densification was found to vary in a 3-7% range depending on the choice of this configuration.

An indirect experimental evidence of the occurrence of phase-transformation/irreversible-densification of soda-lime glass under shock loading in a pressure range around 4 GPa was obtained in the study of Grady and Chhabildas (Ref 27, 28). Specifically, Grady and Chhabildas (Ref 27) observed an unexpectedly low measured particle velocity which they attributed to the interplay of permanent densification or inelastic shear. By carrying out a simple quantitative analysis of the shock wave reflection from the soda-lime interface at which the particle velocity was measured, these authors concluded that the underlying inelastic deformation process would result in a 1.5-2% volume reduction. These findings are in general agreement with those obtained computationally in this study.

As will be shown in the next section, conversion of the pressure versus specific-volume isotherms into the corresponding pressure versus specific-volume Hugoniots and isentropes, requires also the knowledge of the internal energy density, ε, versus specific volume (loading and unloading) isotherms. While, as will be shown in the next section, ε versus *v* isotherm can be derived from the *p* versus *v* isotherm using a procedure based on the first two laws of thermodynamics and on the Maxwell's equations, the former isotherm was obtained along with the *p* versus *v* isotherms using the same molecular-level computational analysis. A plot of the ε versus *v* isotherms is displayed in Fig. 5. The results displayed in Fig. 4 and 5 are
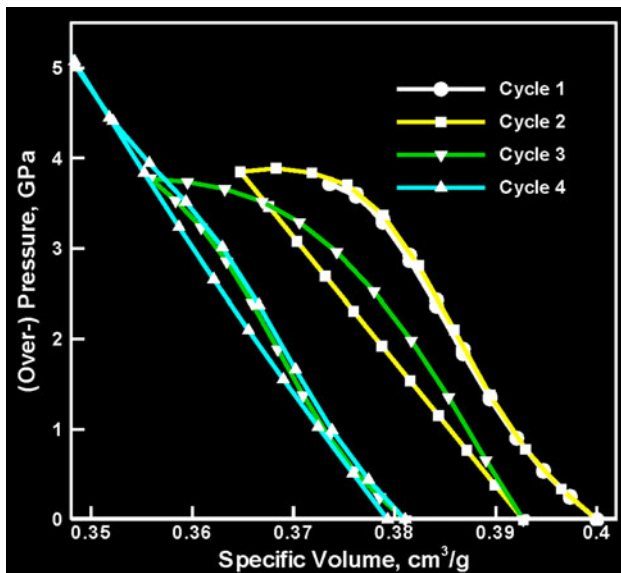

Fig. 4 Typical pressure vs. specific-volume (298 K) loading/un-loading isotherms obtained in the present molecular-level analysis of repeated pressurization/depressurization simulations. In each loading cycle, pressurization was carried out to a higher peak pressure followed by a complete depressurization (i.e., to the atmospheric pressure)

Fig. 5 Typical internal energy density vs. specific-volume (298 K) loading/un-loading isotherms obtained in the present molecular-level analysis of repeated pressurization/depressurization simulations. In each loading cycle, pressurization was carried out to a higher peak pressure followed by a complete depressurization (i.e., to the atmospheric pressure)
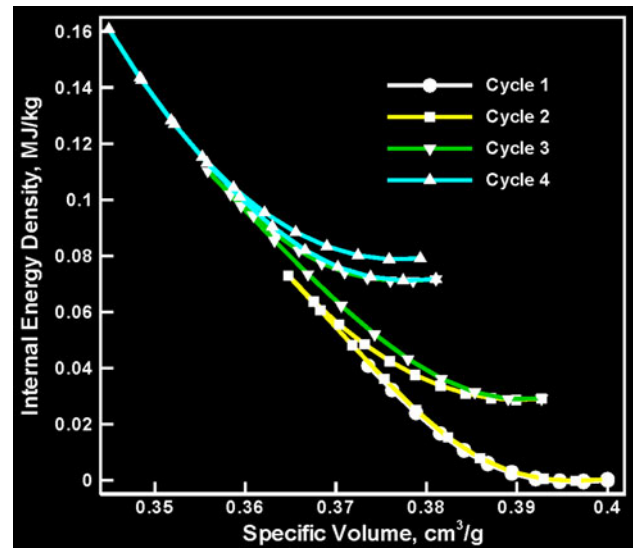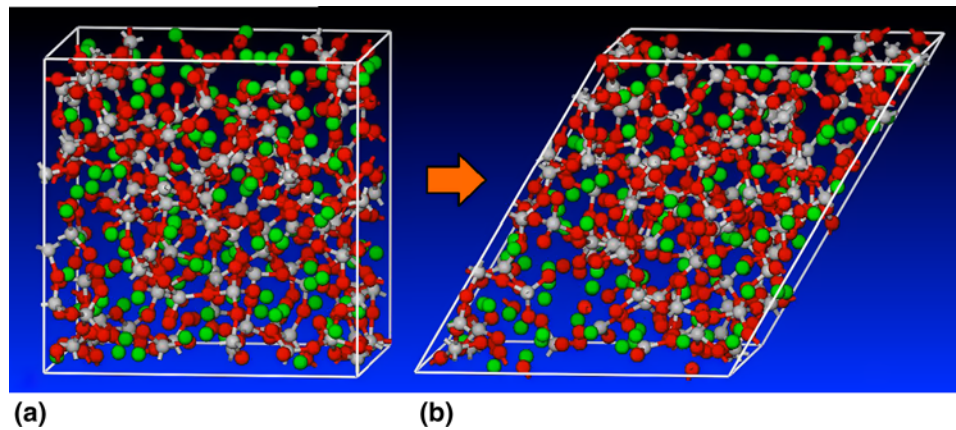
Fig. 6 An example of molecular-level topology evolution accompanying simple-shear mechanical tests

associated with the same set of molecular-dynamics pressurization/de-pressurization runs.

3.2.3 Transformation/Densification-Induced Strengthening. As discussed in section 3.4, simple shear computational mechanical tests are used to assess soda-lime glass strength. An example of the typical molecular-level topology evolution accompanying these tests is displayed in Fig. 6(a)-(b). The computational procedure described in section 3.4 established that, depending on the initial structure of the computational cell, the strength of fully transformed soda-lime glass is higher by 30-50% than that of the virgin material.

4. Isotherm to Hugoniot/Isentrope Conversion

As mentioned earlier, one of the main objectives of this study is to examine the potential of pressure-induced phase-transformation/irreversible-densification in mitigating the effects of shock in ballistic impact. A shock wave (or simply a shock) is a wave which propagates through a medium at a speed higher than the sound speed and its passage causes an abrupt and discontinuous change in the material state variables (e.g., temperature, pressure, density, and internal energy). The magnitude of the state-variable changes and the shock speed increase with the strength of the shock. While acoustic waves give rise to isentropic changes in the material state variables, passage of a shock is typically associated with irreversible (entropy-increasing) changes in the same variables. The reason behind this difference is that shock involves very high strain rates that bring energy-dissipative viscous effects into prominence. As will be shown below, the irreversible nature of the material-state changes brought about by shock passage precludes the p versus v and ε versus v isotherms (obtained in the previous section) from being directly used in the shock propagation/interaction analysis (carried out later in this study).

Before proceeding with the conversion of the loading/unloading isotherms obtained in the previous section into their corresponding Hugoniots and isotherms, it should be noted that the internal energy density has two main contributions: (a) potential-energy contribution associated with bonding and non-bonding interactions between the atomic-scale constituents of the system; and (b) the thermal component which is associated with the vibrational energy of the same constituents. Clearly, specific-volume controls the potential energy part

while temperature has a dominant effect on the thermal part. At non-zero absolute temperatures, both the specific-volume (change) and the internal energy density contribute to the internal pressure in the material. A function which relates pressure, p, specific-volume, v, and the internal energy density, ε, is commonly referred to as an Equation of State (EOS). The EOS is a critical part of a material model for use in (continuum-level) computational investigations of the response of structures to shock loading. In situations in which one is interested only in the problem of shock propagation/interaction in plate-like structures in the presence of uni-axial strain deformation states (as is the present case), a complete definition of the EOS is not required. Instead, a locus of t_{11} versus v versus ε (versus $\dot{x}$-particle velocity versus U_s-shock speed) shocked-material states commonly referred to as a *Hugoniot* is sufficient where t_{11} is the axial stress, and the only non-zero component of strain (the axial strain) is related to the specific-volume. Likewise, to analyze the propagation/interaction of release (decompression) waves under the same geometrical/deformation state conditions, it is sufficient to define the corresponding t_{11} versus v versus ε isentropes.

As a first step toward creating the foregoing Hugoniot/isentrope relations, molecular-scale modeling was employed to obtain $t_{11}^{(\theta)}$ versus v and $\varepsilon^{(\theta)}$ versus v (loading and unloading) isotherms, where superscript θ is used to denote a constant temperature condition. However, these relations define the locus of equilibrium material states under isothermal deformation conditions and could not be directly used in the analysis of shock/release wave propagation/interaction. The main reasons for this limitation are: (a) shock loading is an irreversible process which results in energy dissipation (causing an increase in the shocked-material thermal energy); and (b) shock loading/unloading imparts a significant momentum to the material particles which requires overcoming particle inertial effects. Consequently, at the same level of the compressed-material volume, shocked-material states are associated with higher levels of stress/pressure and internal energy density than their isothermal counterparts. Hence, before the molecular-level isothermal compression relations obtained in the previous section can be used in the analysis of shock propagation/interaction, they must be converted into their respective shock-based Hugoniots/isentropes. Details of this conversion are presented in the remainder of this section. Separate consideration is given to the isotherm conversion to Hugoniots and isentropes.

4.1 Determination of Shock-Loading Hugoniot

The isotherm-to-Hugoniot conversion procedure employed in this study follows closely the one outlined in Ref 29. The first step in this procedure is to separate $t_{11}^{(\theta)} = -p^{(\theta)} + 4\tau_{max}^{(\theta)}/3$ versus v into $p^{(\theta)}$ versus v and $\tau_{max}^{(\theta)}$ versus v relations, where $\tau_{max}^{(\theta)}$ is the maximum shear stress. The next step is to handle the conversion of the latter two isotherms into the corresponding Hugoniots/isentropes separately.

Conversion of the $p^{(\theta)}$ versus v isotherm into the corresponding Hugoniot is rooted in the assumption that the known isotherm and the sought Hugoniot are associated with the same pressure versus density versus internal energy Mie-Gruneisen EOS. If, for a given range of specific-volumes, v, the isotherm in question defines $p^{(\theta)}(v)$ and $\varepsilon^{(\theta)}(v)$ (θ-temperature) set of material states on the EOS surface, then the Hugoniot centered on the initial state $p^{(H)} = 0$, $\varepsilon^{(H)} = \varepsilon_R$ and $v = v_R$ is defined, over the same range of v as:

$$p^{(H)}(v) = p^{(\theta)}(v, \theta_0) + \frac{\gamma(v)}{v}\left[\varepsilon^{(H)}(v) - \varepsilon^{(\theta)}(v, \theta_0)\right] \quad \text{(Eq 5)}$$

where $\gamma = \left.\frac{\partial p}{\partial \varepsilon}\right|_v$ is the Gruneisen gamma. It should be noted that states $p^{(H)}$ and $\varepsilon^{(H)}$ in Eq 5 are mutually related through the Rankine-Hugoniot equation as:

$$\varepsilon^{(H)} - \varepsilon_R = \frac{1}{2}\left(-p^{(H)}\right)\left(-v + v_R\right) \quad \text{(Eq 6)}$$

As far as the $\varepsilon^{(\theta)}$ versus v isotherm is concerned, it was shown (in Fig. 5) that this relation can be obtained directly using the molecular-level computations discussed in the previous section. Alternatively, this relationship can be derived from the $p^{(\theta)}$ versus v isotherm by applying the following two-step procedure: (a) to account for the fact that the internal energy density is a function of specific-volume and entropy (while entropy depends on the specific-volume and temperature), $\frac{\partial \varepsilon^{(\theta)}(v, \eta(v, \theta))}{\partial v}$ is first derived using the chain rule as:

$$\left.\frac{\partial \varepsilon^{(\theta)}}{\partial v}\right|_\theta = \left.\frac{\partial \varepsilon^{(\theta)}}{\partial v}\right|_\eta + \left.\frac{\partial \varepsilon^{(\theta)}}{\partial \eta}\right|_v \left.\frac{\partial \eta}{\partial v}\right|_\theta = -p^{(\theta)} + \theta\left(\frac{\gamma}{v}C^v\right) \quad \text{(Eq 7)}$$

where η is the entropy density. $p^{(\theta)} = -\left.\frac{\partial \varepsilon^{(\theta)}}{\partial v}\right|_\eta$ and $\theta = \left.\frac{\partial \varepsilon^{(\theta)}}{\partial \eta}\right|_v$ relations originate from the combined statement of the first and second laws of thermodynamics $d\varepsilon^{(\theta)} = \theta d\eta - p^{(\theta)}dv$, while $\frac{\gamma}{v}C^v = \left.\frac{\partial \eta}{\partial v}\right|_\theta$ is obtained through the use of Maxwell's equations; and (b) Eq 7 is next integrated between the initial specific-volume, v_0, and current specific-volume, v, as:

$$\varepsilon^{(\theta)}(v, \theta_0) = \varepsilon_0 - \int_{v_0}^{v} p^{(\theta)}(v'; \theta_0)dv' + \frac{\gamma_R}{v_R}C_R^v \theta_0(v - v_0) \quad \text{(Eq 8)}$$

where $\varepsilon_0 = \varepsilon^{(\theta)}(v_0, \eta(v_0, \theta_0))$, $C^v = \left.\frac{\partial \varepsilon}{\partial \theta}\right|_v$ is the constant-volume specific-heat, and θ_0 is the temperature associated with the isotherm in question. By combining Eq 5, 6, and 8 and solving the resulting equation for $p^{(H)}$, one obtains the sought Hugoniot as:

$$p^{(H)}(v) =$$
$$\frac{p^{(\theta)}(v, \theta_0) + \frac{\gamma_R}{v_R}\left[\varepsilon_R - \varepsilon_0 + \int_{v_0}^{v} p^{(\theta)}(v', \theta_0)dv' - \theta_0\frac{\gamma_R}{v_R}C_R^v(v - v_0)\right]}{1 - \frac{\gamma_R}{2v_R}(v_0 - v)}$$
$$\text{(Eq 9)}$$

It should be noted that in Eq 9, it was assumed that $\frac{\gamma}{v}\left(= \frac{\gamma_R}{v_R}\right)$ and C_R^v remain unchanged during shock loading. These assumptions are commonly made in the case of the so-called Gruneisen materials in which gamma is only a function of v. Equation 9 shows that for a given $p^{(\theta)}(v)$ isotherm associated with the initial material states ε_0, θ_0, and v_0 (and defined over a range of v), the corresponding $p^{(H)}(v)$ Hugoniot centered at the initial state (ε_R, v_R) can be obtained (over the same range of v) provided material parameters γ_R and C_R^v are known. In this study, these two parameters are assigned the following values: $\gamma_R = 0.63$ (Ref 30) and $C_R^v = 900$ J/kg·K (Ref 31). These values correspond to the ambient temperature and pressure conditions of glass chosen as the reference state of this material. Equation 9 also shows that it is convenient to make the initial isothermal state of the material and the reference state of the shocked material identical. In this case, $\varepsilon_R = \varepsilon_0$ and Eq 9 becomes somewhat simpler.

As far as the conversion of the $\tau_{max}^{(\theta)}$ versus v relations to $\tau_{max}^{(H)}$ versus v relations, it was assumed that the shock-loading would primarily influence the hydrostatic portion of the stress field. Hence, no conversion of the deviatoric part of the axial stress was carried out. Consequently, $t_{11}^{(H)}(v)$ was obtained by simply adding the $4\tau_{max}^{(H)}(v)/3$ isotherm to the $-p^{(H)}(v)$ Hugoniot.

4.2 Determination of the Release-Wave Unloading Isentrope

The analysis presented above allows the conversion of a loading isotherm to the corresponding loading Hugoniot. Following the procedure described by Davison (Ref 29), it can be readily shown that high-rate unloading associated with the propagation of release/rarefaction waves is an adiabatic/isentropic process. Hence, to analyze propagation of these waves in plate-like structures associated with uni-axial strain deformation, one must convert unloading isotherms (obtained via the molecular-level simulations) into the corresponding isentropes. The conversion procedure used here is quite similar to the foregoing isotherm-to-Hugoniot conversion procedure and involves the following steps:

(a) an equation analogous to Eq. 5 is first constructed in which the Hugoniot quantities are replaced with their isentropic counterparts, $p^{(\eta)}$ and $\varepsilon^{(\eta)}$;

(b) in this equation, $\varepsilon^{(\theta)}(v)$ is again expressed using Eq 8; and

(c) $\varepsilon^{(\eta)}(v)$ is obtained using a procedure analogous to that employed during the derivation of Eq 8 to yield:

$$\varepsilon^{(\eta)}\left(v; \eta_R^{(\eta)}\right) = \varepsilon_R^{(\eta)} - \int_{v_R^{(\eta)}}^{v} p^{(\eta)}\left(v'; \eta_R^{(\eta)}\right)dv' \quad \text{(Eq 10)}$$

where $\eta_R^{(\eta)}$ is the constant/reference value of the entropy density along the isentrope. Since Eq 10 contains the unknown function $p^{(\eta)}(v; \eta_R^{(\eta)})$, the equation mentioned in (a) cannot be used to simply compute $p^{(\eta)}$ by evaluating the right-hand side of this equation. To overcome this problem, this equation is differentiated with respect to v to yield the following linear, first order, ordinary differential equation with constant coefficients:

$$\frac{\partial p^{(\eta)}}{\partial v} + \frac{\gamma_R}{v_R}p^{(\eta)} = \frac{\partial p^{(\theta)}}{\partial v} + \frac{\gamma_R}{v_R}p^{(\theta)} - \left(\frac{\gamma_R}{v_R}\right)^2 C_R^v \theta_R^{(\theta)} \quad \text{(Eq 11)}$$

This equation can be readily integrated numerically to yield $p^{(\eta)}(v)$. However, it should be noted that the unloading isotherm associated with the same temperature, θ_0, as the loading isotherm cannot be used here. The reason for this is that shock is accompanied with energy dissipation so that the shocked-material temperature is normally higher than the temperature in the material's reference state. Hence, isothermal unloading would take place along a $\theta_R^{(\eta)} > \theta_0$ isotherm. This isotherm can be obtained using the known θ_0 unloading isotherm (generated using the molecular level simulations) and by integrating $\left.\frac{\partial p}{\partial \theta}\right|_v = \frac{\gamma_R}{v_R} C_R^v$ to obtain:

$$p^{(\theta)}\left(v; \theta_R^{(\eta)}\right) = p^{(\theta)}(v; \theta_0) + \frac{\gamma_R}{v_R} C_R^v\left(\theta_R^{(\eta)} - \theta_0\right) \quad \text{(Eq 12)}$$

The foregoing procedure yields a $p^{(\eta)}(v; \eta_R^{(\eta)})$ isentrope. To obtain the corresponding $t_{11}^{(\eta)}(v; \eta_R^{(\eta)})$ relation, a procedure analogous to the one used in the case of shock-loading Hugoniot was used.

4.3 Results and Discussion

By employing the procedures described in the previous two sections, the axial stress versus specific-volume isotherms obtained via the use of molecular-level simulations are converted into the respective Hugoniots and isentropes. The results obtained are summarized in Fig. 7(a). Since $t_{11}^{(H)}$ versus $\dot{x}$ Hugoniots are generally quite beneficial in the analysis of shock reflection/transmission, these relations are also generated by combining the $t_{11}^{(H)}$ versus v Hugoniots with the corresponding jump equations. The results of this procedure are depicted in Fig. 7(b). As will be shown in the next section, changes in the soda-lime glass Hugoniots brought about by the pressure-induced phase-transformations/irreversible-densifications may significantly affect the shock-mitigation ability of this material.

5. Analysis of Shock Mitigation in Soda-Lime Glass

In this section, an attempt is made to assess (and, wherever possible, quantify) the effect of ca. 4 GPa pressure-induced phase-transformation/irreversible-densification in soda-lime glass on its ability to mitigate the effects of shock loading. Specifically, in addition to analyzing how irreversible densification affects the strength/speed of shocks, the effect of the same phenomenon on the propagation/interaction of release waves is also analyzed. These waves are typically generated as a result of shock reflection at material interfaces (e.g., glass/polycarbonate interface in laminated transparent-armor systems) and free surfaces. Furthermore, the ability of pressure-induced phase-transformation/irreversible-densification to absorb/dissipate (kinetic) energy accompanying shock loading is also discussed in this section.

5.1 Shock Propagation in Soda-Lime Glass

In many respects, the occurrence of pressure-induced phase transformations in soda-lime glass at sufficiently high levels of pressure is analogous to the occurrence of plasticity in metals under sufficiently high levels of equivalent (deviatoric) stress. Consequently, some similarities relative to the propagation, transmission/reflection, and interaction of shocks and release
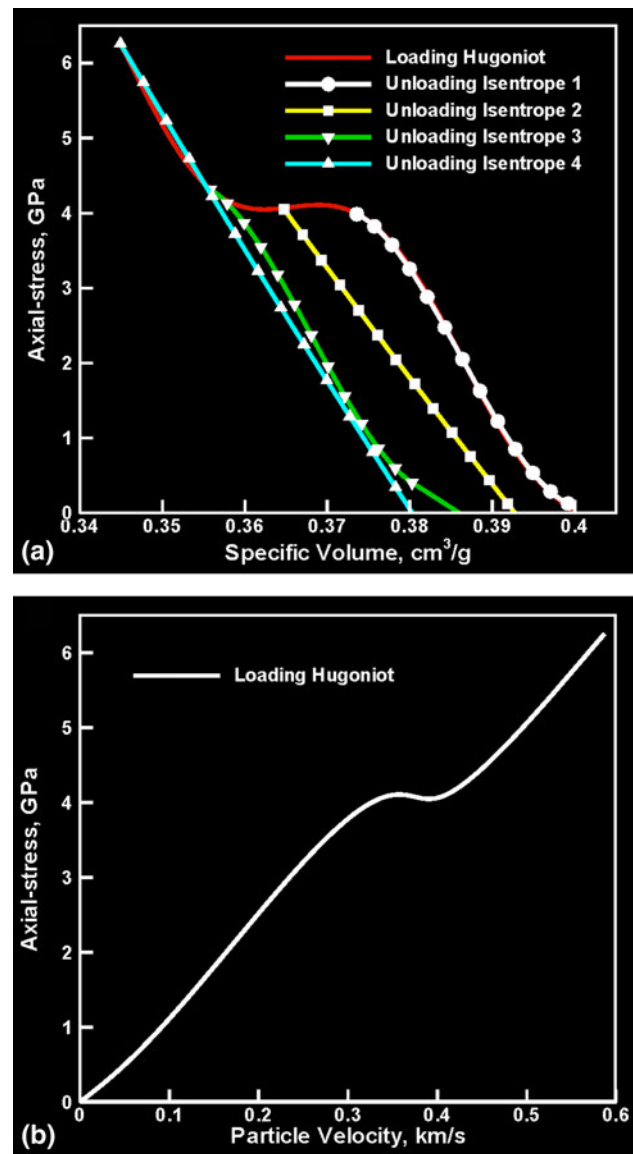

Fig. 7 (a) Axial-stress versus specific-volume, and (b) axial-stress vs. particle-velocity Hugoniot and isentrope relationships for soda-lime glass undergoing pressure-induced phase-transformation/irreversible-densification

waves should be expected in the two cases. To facilitate the present analysis of shock propagation/interaction in soda-lime glass, a schematic of the $p^{(H)}$ versus v Hugoniot for soda-lime glass is provided in Fig. 8(a). For comparison, the Hugoniot of a hypothetical "non-transforming" soda-lime glass is also depicted in this figure. The initial ("down-stream") state of material is denoted as point A.

The first similarity between shock-induced plasticity and shock-induced irreversible densification is that, shocks propagate not as single waves (which would produce a single upstream material states such as the one denoted by point B in Fig. 8a) but rather in pairs. The leading shock, the so-called elastic precursor, shocks the material to the state at which the conditions for the onset of phase-transformation are met (point C in Fig. 8a). The trailing shock, the so-called plastic shock, then gives rise to the transformed/densified material state (point D in Fig. 8a).
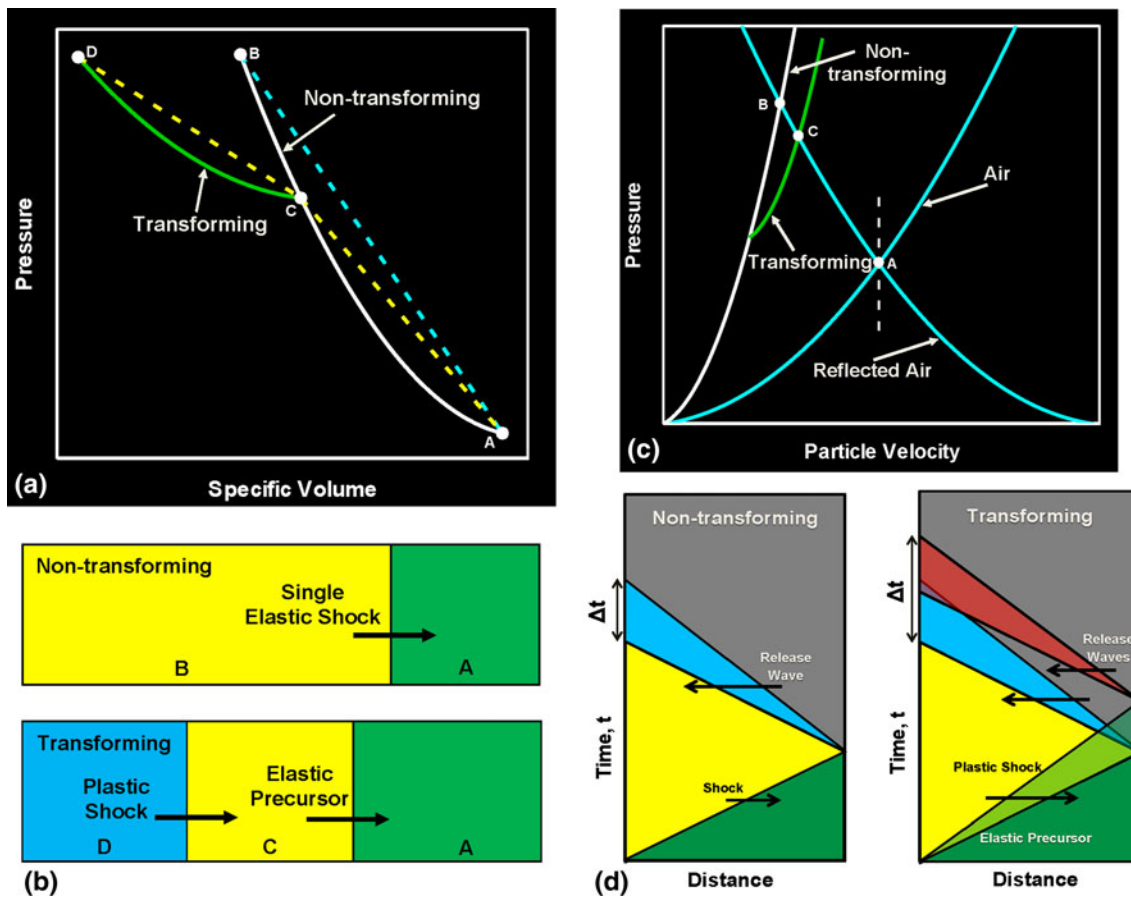
Fig. 8 Various Hugoniots and characteristic plots used in the analysis of shock and release wave propagation through a non-transforming and a transforming soda-lime glass (see text for details)

Since the "plastic shock" travels at a substantially lower speed, the accompanying stress rates are significantly reduced relative to the case of a "purely elastic" single shock (the shock speeds scale with the magnitude of the slope of the corresponding (AB, AC, and CD) Rayleigh lines in Fig. 8a). This helps the material maintain its structural integrity (i.e., the probability of cracking is significantly reduced) and ensures functional performance (optical clarity) of the transparent-armor structure. A schematic is provided in Fig. 8(b) to depict the observed differences in shock wave propagation through "non-transforming" and "transforming" soda-lime glass.

It should be noted that the analysis presented above was carried out under the assumption that shock loading is associated with the same "up-stream" pressure-level in both the "transforming" and the "non-transforming" soda-lime glass. However, due to differences in the Hugoniots of these two materials, this assumption may not be generally valid. To determine differences in the "up-stream" pressure-levels for the two materials (under the constant blast-loading conditions), a schematic of the $p^{(H)}$ versus $\dot{x}$ Hugoniot is depicted in Fig. 8(c). In addition, the Hugoniot of air is also depicted in this figure and point A is used to denote the air-borne shock state. By employing the so-called impedance matching method (which involves mirroring the air Hugoniot about a vertical line through the shock state A and finding the points of intersection between the mirrored Hugoniot and the two soda-lime glass Hugoniots), the "transmitted" shock states within

soda-lime glass can be determined. These states are denoted, in Fig. 8(c), using points B and C for the "non-transforming" and the "transforming" soda-lime glass, respectively. It is seen that somewhat lower "up-stream" pressure accompanies shock loading of the "transformed" soda-lime glass. This finding points toward yet another potential way in which pressure-induced phase-transformations in soda-lime glass can help mitigate the effects of shock loading.

5.2 Release-Wave Propagation in Soda-Lime Glass

In laminated (multi-layer) transparent armor structures, initial shock loading results, through multiple wave reflection/transmission/interaction, in a number of shock and release waves propagating at any instant of time in any of the armor laminae. When two approaching release waves intersect, the material bounded by the two resulting release waves travelling away from each other may be subjected to tension. If the attendant tensile stresses exceed the material fracture strength, fracture/spall may take place causing a loss in optical clarity/functional performance of the transparent armor structure.

As discussed in section 3, molecular-level simulation results of soda-lime glass shear response under pressure revealed that pressure-induced phase-transformations/irreversible-densification increases the shear strength of the material. While fracture of glass could not be modeled directly using the present molecular-level computational approach, it is anticipated that an

increase in shear strength of the soda-lime glass due to pressure-induced irreversible-densification will result in a similar increase in the material fracture strength. This is another potential way in which pressure-induced phase-transformation/irreversible-densification can improve shock mitigation performance of soda-lime glass.

Another potential mechanism for reduction of the fracture/spall propensity in shock-loaded glass is associated with greater dispersion (i.e., increased profile width) of the reflected release waves. In simple terms, if two intersecting release waves are more dispersed, lower values of the peak tensile stress and/or lower volume of the material subjected to the peak tensile stresses are expected. To determine if pressure-induced phase-transformations in soda-lime glass promote release wave dispersion, schematics of the time versus distance (characteristic analysis) plots are depicted in Fig. 8(d) for the two cases of soda-lime glass. In the "non-transforming" soda-lime case, a single shock originating at the left surface of the glass panel at zero time traverses the panel and reflects from the right panel surface as a release wave. The difference in the arrival times of the trailing and the leading characteristics of this wave to the left panel surface can then be used as a measure of the release wave dispersion. In the case of a "transforming" soda-lime glass, a pair of shocks is generated at the left panel surface and each shock generates a separate release wave upon reflection from the panel right surface. Clearly, the width of the combined rarefaction wave (defined now as the difference in the arrival time of the "plastic shock" release wave trailing edge and the "elastic precursor" release wave leading edge) is greater suggesting another potential mechanism by which high-pressure densification of soda-lime glass may mitigate shock loading effects.

5.3 Energy-Absorption Capacity of Soda-Lime Glass

Simple examination of the pressure versus specific-volume Hugoniot displayed in Fig. 7(a) suggests that ca. 4 GPa pressure-induced phase-transformation/irreversible-densification may yield additional important benefits with respect to mitigating the effects of shock loading. While analyzing Fig. 7(a), it should be recalled that shock-loading takes place along the Rayleigh line(s) connecting the material initial and shocked states, while release-wave unloading takes place along an isentrope. Hence, the area bounded by the Rayleigh line(s), the corresponding isentrope and the v axis, defines the energy absorbed/dissipated in the material which was initially loaded by the passage of a shock and subsequently unloaded by the passage of a release wave. To provide a semi-quantitative assessment of the enhanced energy absorption/dissipation potential of soda-lime glass undergoing pressure-induced phase-transformation/irreversible-densification, a hypothetical Hugoniot and the corresponding isentropes are considered for the non-transforming soda-lime glass. These hypothetical curves are not drawn in Fig. 7(a) to preserve clarity. Nevertheless, it is obvious that the energy absorption/dissipation capacity of the "transforming" soda-lime glass is substantially higher than that of its hypothetical "non-transforming" counterpart. By comparing the corresponding areas between the Rayleigh line(s) and the isentropes for the fully transformed and "non-transforming" soda-lime glass in Fig. 7(a), it was estimated that phase-transformation can increase energy absorption capacity of soda-lime glass by 6-7 times. This is clearly a finding which warrants closer examination in our future study since it may lead to substantial improvements in shock-mitigation performance of transparent armor systems.

5.4 Structure/Component-Performance-Driven Material Design

The study overviewed in the present manuscript clearly revealed that (ca. 4 GPa) pressure-induced phase-transformations and the accompanying irreversible-densification can have a beneficial role in regard to mitigating the effects of ballistic/blast-impact-induced shocks in soda-lime-based transparent armor structures. Since similar phase-transformations and irreversible-densification phenomena were not found in either fused-silica or borosilicate glass (a part of the ongoing work based on the use of the same molecular-level computational method), it is clear that glass chemistry and microstructure play an important role in the behavior of SiO_2-based amorphous materials under high pressures. A possible explanation for the observed differences in the high-pressure behavior of soda-lime, fused-silica and borosilicate glass can be attributed to expected differences in the nature of their random network of SiO_4^{4-} tetrahedra. As discussed in section 2, soda-lime glass is associated with a more-open random network due to the presence of network modifiers (Na_2O and CaO). The results obtained in this study then suggest that, under relatively modest pressures of ca. 4 GPa, material (irreversible) densification can take place resulting in the formation of a material with a more compacted random network. In the case of fused-silica and borosilicate glass, zero-pressure random network is already quite compacted so that no measurable densification takes place at ca. 4 GPa pressure level. In these glasses (as well as in soda-lime glass), densification takes place at substantially higher pressures and involves not simple bonding changes in the SiO_4^{4-} glass network, but the generation of a stishovite phase composed of SiO_6^{6-} octahedrons.

Returning to the problem of ca. 4 GPa pressure-induced phase-transformation/irreversible-densification in soda-lime glass, it should be noted that while the presence of the more open random network may be beneficial from the shock-mitigation point of view, this effect must be balanced against the accompanying reduction in the virgin material fracture strength. The latter effect may lead to spall/cracking-resistance loss in soda-lime glass and the associated loss of optical clarity (an example of the functional failure of a transparent-armor structure). In other words, as potential modifications in soda-lime glass are being considered in an attempt to maximize its shock-mitigation potential, one must monitor the effect of these modifications on the material fracture strength. This is a prototypical example of the "materials-by-design" approach within which structure/component performance assessment is used to guide the design (and processing/synthesis) of materials which maximize such performance. It should be noted that the virgin material fracture strength is not of major importance in the case of blast-loaded glass panels in which tensile loading is normally preceded by compressive shock loading (which as shown here), gives rise to the material-densification induced strengthening. On the other hand, in the case of ballistic impact, radial tensile shocks are often induced which may cause the formation of so-called ring cracks. In this case, the virgin material fracture strength is an important material selection parameter which controls the initial ballistic-penetration resistance.

6. Summary and Conclusions

Based on the results obtained in this study, the following summary remarks and main conclusions can be made:

1. Molecular-level modeling of soda-lime glass revealed the occurrence of an irreversible-densification process when the pressure exceeds ca. 4 GPa. Close examination of molecular-level topology revealed that this process is associated with an increase in the average coordination number of the silicon atoms, and the creation of two to fourfold (smaller, high packing-density) Si-O rings.
2. A series of loading/unloading/reloading computational experiments is carried out in order to generate the appropriate 298 K pressure versus specific-volume isotherms.
3. These isotherms are next converted into the corresponding (pressure versus specific-volume and pressure versus particle velocity) loading Hugoniots and unloading isentropes.
4. The obtained Hugoniot and isentrope relations are used to semi-quantitatively assess the potential of pressure-induced phase transformation in soda-lime glass for mitigating shock-loading effects. This procedure identified several beneficial effects of the pressure-induced phase transformation in soda-lime glass such as lowering of the loading/unloading stress-rates and stresses, shock/release-wave dispersion, and energy absorption associated with the study of phase-transformation.

Acknowledgments

References

1. E. Strassburger, P. Patel, W. McCauley, and D.W. Templeton, Visualization of Wave Propagation and Impact Damage in a Polycrystalline Transparent Ceramic-AlON, *Proceedings of the 22nd International Symposium on Ballistics*, November 2005, Vancouver, Canada
2. AMPTIAC Quarterly: *Army Materials Research: Transforming Land Combat Through New Technologies*, 8 (No. 4), 2004
3. E. Strassburger, P. Patel, J.W. McCauley, C. Kovalchick, K.T. Ramesh, and D.W. Templeton, High-Speed Transmission Shadowgraphic and Dynamic Photoelasticity Study of Stress Wave and Impact Damage Propagation in Transparent Materials and Laminates Using The Edge-on Impact Method, *Proceedings of the 23rd International Symposium on Ballistics*, Spain, April 2007
4. D.Z. Sun, F. Andreiux, and A. Ockewitz, Modeling of the Failure Behavior of Windscreens and Component Tests, *4th LS-DYNA Users' Conference*, Bamberg, Germany, 2005
5. L.V. Woodcock, C.A. Angell, and P. Cheeseman, Molecular Dynamics Studies of the Vitreous State: Simple Ionic Systems and Silica, *J. Chem. Phys.*, 1976, **65**, p 1565–1577
6. R.G.D. Valle and E. Venuti, High-Pressure Densification of Silica Glass: A Molecular-Dynamics Simulation, *Phys. Rev. B*, 1996, **54**(6), p 3809–3816
7. K. Trachenko and M.T. Dove, Densification of Silica Glass Under Pressure, *J. Phys. Condens. Matter*, 2002, **14**, p 7449–7459
8. Y. Liang, C.R. Miranda, and S. Scandolo, Mechanical Strength and Coordinate Defects in Compressed Silica Glass: Molecular Dynamics Simulations, *Phys. Rev. B*, 2007, **75**, p 024205
9. B. Nghiem, PhD thesis, University of Paris 6, France 1998
10. C. Denoual and F. Hild, Dynamic Fragmentation of Brittle Solids: A Multi-scale Model, *Eur. J. Mech. Solids A*, 2002, **21**, p 105–120
11. M. Yazdchi, S. Valliappan, and W. Zhang, A Continuum Model for Dynamic Damage Evolution of Anisotropic Brittle Materials, *Int. J. Numer. Methods Eng.*, 1996, **39**, p 1555–1583
12. F. Hild, C. Denoual, P. Forquin, and X. Brajer, On the Probabilistic and Deterministic Transition Involved in a Fragmentation Process of Brittle Materials, *Comput. Struct.*, 2003, **81**, p 1241–1253
13. M. Grujicic, B. Pandurangan, N. Coutris, B.A. Cheeseman, C. Fountzoulas, P. Patel, and E. Strassburger, A Ballistic Material Model for Starphire®, A Soda-lime Transparent Armor Glass, *Mater. Sci. Eng. A*, 2008, **492**(1), p 397–411
14. M. Grujicic, B. Pandurangan, W.C. Bell, N. Coutris, B.A. Cheeseman, C. Fountzoulas, and P. Patel, An Improved Mechanical Material Model for Ballistic Soda-Lime Glass, *J. Mater. Eng. Perform.*, 2009, **18**(8), p 1012–1028
15. M. Grujicic, B. Pandurangan, N. Coutris, B.A. Cheeseman, C. Fountzoulas, and P. Patel, A Simple Ballistic Material Model for Soda-Lime Glass, *Int. J. Impact Eng.*, 2009, **36**, p 386–401
16. T.J. Holmquist, D.W. Templeton, and K.D. Bishnoi, Constitutive Modeling of Aluminum Nitride for Large Strain High-strain Rate, and High-pressure Applications, *Int. J. Impact Eng.*, 2001, **25**, p 211–231
17. G.T. Camacho and M. Ortiz, Computational Modeling of Impact Damage in Brittle Materials, *Int. J. Solids Struct.*, 1996, **33**(20–22), p 2899–2938
18. W.D. Kingery, H.K. Bowen, and D.R. Uhlmann, *Introduction to Ceramics*, 2nd ed., Wiley, New York, 1976, p 91–124
19. http://www.accelrys.com/mstudio/msmodeling/visualiser.html
20. http://www.accelrys.com/mstudio/msmodeling/amorphouscell.html
21. H. Sun, COMPASS: An ab Initio Force-Field Optimized for Condensed-Phase Applications Overview with Details on Alkane and Benzene Compounds, *J. Phys. Chem. B*, 1998, **102**, p 7338–7364
22. H. Sun, P. Ren, and J.R. Fried, The COMPASS Force Field: Parameterization and Validation for Phosphazenes, *Comput. Theor. Polym. Sci.*, 1998, **8**(1/2), p 229–246
23. M. Grujicic, Y.-P. Sun, and K. Koudela, The Effect of Covalent Functionalization of Carbon Nanotube Reinforcements on the Atomic-Level Mechanical Properties of Poly-Vinyl-Ester-Epoxy, *Appl. Surf. Sci.*, 2007, **253**, p 3009–3021
24. http://www.accelrys.com/mstudio/msmodeling/discover.html
25. S. Nose, A Unified Formulation of the Constant Temperature Molecular Dynamics Methods, *J. Chem. Phys.*, 1984, **81**, p 511–519
26. M. Grujicic, B. Pandurangan, C.D. Angstadt, K.L. Koudela, and B.A. Cheeseman, Ballistic Performance Optimization of a Hybrid Carbon Nanotube/E-Glass Reinforced Poly-Vinyl-Ester-Epoxy Matrix Composite Armor, *J. Mater. Sci.*, 2007, **42**, p 5347–5349
27. D.E. Grady and L.C. Chhabildas, *Shock-wave Properties of Soda-lime Glass*, Report No: SAND96-2571C, 1996
28. C.S. Alexander, L.C. Chhabildas, W.D. Reinhart, and D.W. Templeton, Changes to the Shock Response of Fused Quartz due to Glass Modification, *Int. J. Impact Eng.*, 2008, **35**, p 1376–1385
29. L. Davison, *Fundamentals of Shock-wave Propagation in Solids. Shock-wave and High Pressure Phenomena*, Springer, Berlin, Heidelberg, 2008
30. Y. Sato and O.L. Anderson, A Comparison of the Acoustic and Thermal Gruneisen Parameters for Three Glasses at Elevated Pressure, *J. Phys. Chem. Solids*, 1980, **41**(4), p 401–410
31. Cambridge Engineering Selector, http://www.grantadesign.com/